

JGR Space Physics

RESEARCH ARTICLE

10.1029/2024JA033460

Key Points:

- The evolution of the reconnection rate of non-steady-state reconnection is consistent with the energy conversion process in the electron diffusion region (EDR)
- In the stage when the reconnection rate sharply rises, the magnetic energy in the EDR reduces. Meanwhile, electrons and ions are depleted
- The velocity distributions of electrons and ions in the EDR become anisotropic, verifying that they are accelerated and heated

Correspondence to:

S. Lu and Q. Lu,
lusan@ustc.edu.cn;
qmlu@ustc.edu.cn

Citation:

Shu, Y., Lu, S., Lu, Q., & Wang, R. (2025). Evolution of energy conversion and particle behavior in the electron diffusion region during non-steady-state magnetic reconnection. *Journal of Geophysical Research: Space Physics*, 130, e2024JA033460. <https://doi.org/10.1029/2024JA033460>

Received 21 OCT 2024

Accepted 24 APR 2025

Evolution of Energy Conversion and Particle Behavior in the Electron Diffusion Region During Non-Steady-State Magnetic Reconnection

Yukang Shu¹ , San Lu^{1,2,3} , Quanming Lu^{1,2,3} , and Rongsheng Wang^{1,2,3} 

¹CAS Key Laboratory of Geospace Environment, School of Earth and Space Sciences, University of Science and Technology of China, Hefei, China, ²CAS Center for Excellence in Comparative Planetology, Hefei, China, ³Collaborative Innovation Center of Astronautical Science and Technology, Harbin, China

Abstract As a ubiquitous process in plasma environments, magnetic reconnection is responsible for releasing magnetic energy and energizing charged particles. However, the evolution of energy conversion and particle behavior in non-steady-state reconnection is poorly understood. Through particle-in-cell simulation, we present the energy conversion process in the electron diffusion region (EDR) during the temporal evolution of a spontaneous reconnection process under non-steady-state conditions. Our results suggest that the non-steady-state energy conversion pattern presents distinct features at different stages. Moreover, particle motions and their distributions also show various levels of anisotropy at different times. By examining the energy conversion equations and distribution functions, we show how and when electrons and ions become significantly anisotropic over time. The most drastic changes in energy conversion and particle behavior happen at the stage when the reconnection rate sharply rises; meanwhile, a large proportion of mass and energy is expelled from the EDR via enthalpy flux and bulk kinetic energy transport. Our results stress the non-steady-state nature of magnetic reconnection. These features can be vital to the development of the fast reconnection rate, which may further determine the energy conversion of the overall reconnection process.

1. Introduction

Magnetic reconnection is a fundamental process in the space environment, during which the topology of magnetic field lines changes while the magnetic energy is released and plasma is accelerated and heated. Magnetic reconnection occurs in various plasma environments and is related to vital processes such as solar flares and coronal mass ejections (Bárta et al., 2011; Lin & Forbes, 2000; Takasao et al., 2012) in the solar atmosphere, and interaction between the solar wind and planetary magnetosphere (Burch & Phan, 2016; Fuselier et al., 2020; Q. Lu et al., 2022; R. Wang et al., 2010; S. Wang et al., 2020), related to the substorms (Angelopoulos et al., 2008; Baker et al., 1996; Kepko et al., 2015). Furthermore, the process also occurs in the ground experimental facilities (Dorfman et al., 2014; Nagayama et al., 1996; Ren et al., 2005; Sang et al., 2022; Tharp et al., 2012; Weston, 1990; Yamada et al., 1994). Magnetic reconnection is responsible for particle energization in space environments.

Models of magnetic reconnection usually assume reconnection reaches a steady state. Most of those models focus on a specific time to investigate the force balance or energy transfer but omit the time evolution during the process. Recent theoretical works suggest the geometry of the diffusion region of magnetic reconnection determines how fast reconnection proceeds, that is, the reconnection rate (Y. H. Liu et al., 2017, 2022), verifying that the reconnection rate is at the order of 0.1 in the steady-state assumption (Cassak et al., 2017; Shay et al., 1999). However, magnetic reconnection has been detected to be unsteady in various plasma environments in nature (Angelopoulos et al., 2013; H. S. Fu et al., 2013; Imada et al., 2007; Sitnov et al., 2009). Simulations have also found that the structures of the diffusion region and the parameters of the fields and plasmas can change over time (C. Huang et al., 2020; Q. Lu et al., 2013; Sitnov et al., 2009; Wan & Lapenta, 2008). Even though time derivative terms are much smaller than other terms in energy conversion equations (Birn & Hesse, 2005, 2010), the reconnection process still shows distinct non-steady-state features that a moving front is generated in the exhaust region as reconnection develops (Angelopoulos et al., 2013; Deng et al., 2010; S. Lu et al., 2015; Runov et al., 2011; Sitnov et al., 2009; Yi et al., 2019). Along with the pileup front, the outflow of energy flux (including the Poynting flux, bulk kinetic energy flux, and enthalpy flux of particles) can be detected (Aunai et al., 2011;

Eastwood et al., 2013, 2020; S. Lu et al., 2013; Shu et al., 2021, 2022; L. Wang et al., 2020). These results suggest that the energy conversion process in magnetic reconnection is in a non-steady state.

In non-steady-state reconnection, energy conversion in the vicinity of the X-line, that is, the diffusion region, is vital to the whole reconnection process. Energy conversion and particle behavior in this region can impact the energy outflow and development of the reconnection rate. Former investigations show that ions tend to gain more energy than electrons during the overall process (Aunai et al., 2011; Eastwood et al., 2013; Shu et al., 2021; Yamada et al., 2014), whereas the electron energy flux becomes more prominent when drawing closer to the electron diffusion region (EDR) (Eastwood et al., 2020). This suggests electron transport can be significant to the development of reconnection. It has been found that electron bulk kinetic energy and electron enthalpy flux are not equally partitioned during reconnection (S. Lu et al., 2013). The electron energy flux, especially the enthalpy flux, tends to dominate in the EDR (Fargette et al., 2024). Moreover, particles are energized, and their velocity distributions become non-Maxwellian (Bessho et al., 2016; Bourdin, 2017; Cazzola et al., 2016; C. Huang et al., 2010; K. Huang et al., 2021; Li et al., 2019; Scudder & Daughton, 2008). However, it remains unclear how particles behave in different stages of the non-steady-state magnetic reconnection.

To unveil the energy conversion and particle behavior in nonsteady magnetic reconnection, we conducted a two-dimensional particle-in-cell (PIC) simulation. The changes of particle behavior in velocity space are shown during the process of magnetic energy release and particle energization accordingly. Those results can provide some hints related to the evolution of the reconnection rate from the perspective of energy conversion.

2. Simulation Setup

In our simulation, the code we use is an open-source PIC code, EPOCH (Extendable PIC Open Collaboration) code (Arber et al., 2015). The mass ratio between ion and electron is $m_i/m_e = 100$. The initial temperature ratio is $T_i/T_e = 4$. We set $\omega_{pe}/\Omega_e = 2$, where $\omega_{pe} \equiv \sqrt{n_0 e^2 / \epsilon_0 m_e}$ is the electron plasma frequency and $\Omega_e \equiv eB_0/m_e$ is the electron cyclotron frequency. n_0 denotes the peak number density of the current sheet and B_0 is the asymptotic magnetic field.

The calculation domain is set in an x - z plane, where the size of the domain is $L_x \times L_z = 20d_i \times 20d_i$ discretized by 800×800 cells. $d_i \equiv c/\omega_{pi}$ is the ion inertial length and $\omega_{pi} \equiv \sqrt{n_0 e^2 / \epsilon_0 m_i}$ is the ion plasma frequency. We placed 400 pseudo-particles per cell on average. The time step is $\Delta t = 8 \times 10^{-4} \Omega_i^{-1}$, where $\Omega_i \equiv eB_0/m_i$ is the ion cyclotron frequency. The initial configuration is a Harris equilibrium without any initial perturbation, so spontaneous magnetic reconnection can be developed. The magnetic field structure is $\mathbf{B} = B_0 \tanh(z/\delta_0) \mathbf{e}_x$, where $\delta_0 = 0.5d_i$ is the half-width of the initial Harris current sheet. The plasma number density is $n = n_0 \operatorname{sech}^2(z/\delta_0) + n_b$, where $n_b = 0.1$ is the uniform background number density. The x boundary condition is periodic and the z boundary is the perfect electric conductor.

3. Results

3.1. Overview of Energy Conversion in the EDR

The fast reconnection process in our simulation is triggered spontaneously since $\Omega_i t \approx 30$. The out-of-plane component of the electric field E_y , that is, the reconnection electric field, emerges at the X-line (see Figures 1 and a1). As reconnection proceeds, the electric field is enhanced and expands to a wider range, including the pileup region where the reconnected magnetic field B_z strengthens. The peak of the electric field is transferred from the X-line to the pileup region, where the B_z component strengthens and expands over time (Figures 1 and b2–b4). During the expansion, the propagation of the reconnected magnetic field lines forms the Poynting flux in the outflow direction shown in Figures 1d1–d4. Meanwhile, the range of the inner EDR, where the non-ideal electric field component $(\mathbf{E} + \mathbf{V}_e \times \mathbf{B})_y$ is positive (Karimabadi et al., 2007; Shay et al., 2007), remains approximately unchanged during this period, shown in Figures 1 and c1–c4. Since the outer EDR region is not the focus of this research, the EDR mentioned in this paper refers to the inner EDR unless specially noted. The evolution of the reconnection process is consistent with previous studies (Bessho et al., 2018; Daughton et al., 2006; Goldman et al., 2016; Karimabadi et al., 2007; Payne et al., 2024). The development of the reconnection rate during its growth phase is closely related to this region. Thus, we manage to quantify the energy conversion in the EDR by

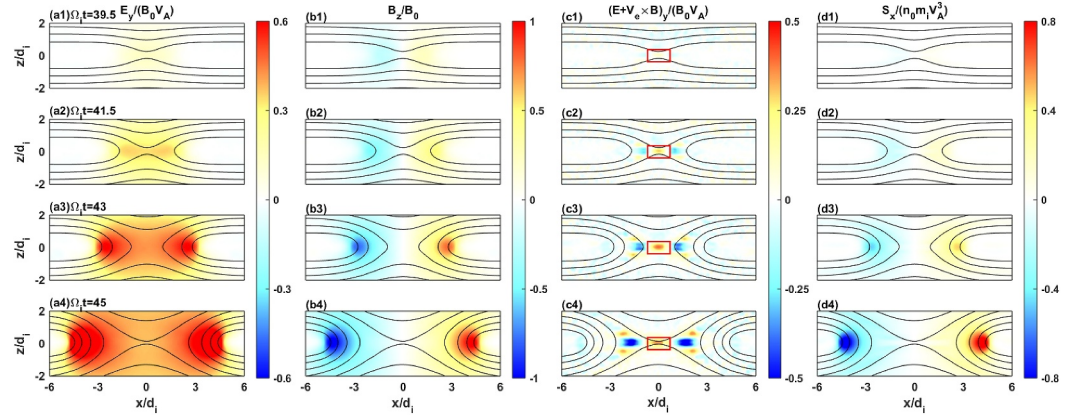


Figure 1. Overview of (a1–a4) the electric field component E_y , (b1–b4) the magnetic field component B_z , (c1–c4) the non-ideal electric field component $(\mathbf{E} + \mathbf{V}_e \times \mathbf{B})_y$, and (d1–d4) Poynting flux outflow S_x at $\Omega_i t = 39.5, 41.5, 43$, and 45 . The red boxes in subfigures c1–c4 enclose the range of the electron diffusion region, whose size remains unchanged ($1.4d_i \times 0.75d_i$) during this period.

integrating the energy conversion equations shown below over a fixed box enclosing the EDR (see the red box in Figures 1 and c1–c4).

$$\frac{\partial W_B}{\partial t} + \frac{\partial W_E}{\partial t} + \nabla \cdot \mathbf{S} + \mathbf{J} \cdot \mathbf{E} = 0 \quad (1)$$

$$\frac{\partial K_\alpha}{\partial t} + \nabla \cdot (K_\alpha \mathbf{V}_\alpha) + (\nabla \cdot \mathbf{P}_\alpha) \cdot \mathbf{V}_\alpha - \mathbf{J}_\alpha \cdot \mathbf{E} = 0 \quad (2)$$

$$\frac{\partial U_\alpha}{\partial t} + \nabla \cdot \mathbf{H}_\alpha + \nabla \cdot \mathbf{Q}_\alpha - (\nabla \cdot \mathbf{P}_\alpha) \cdot \mathbf{V}_\alpha = 0 \quad (3)$$

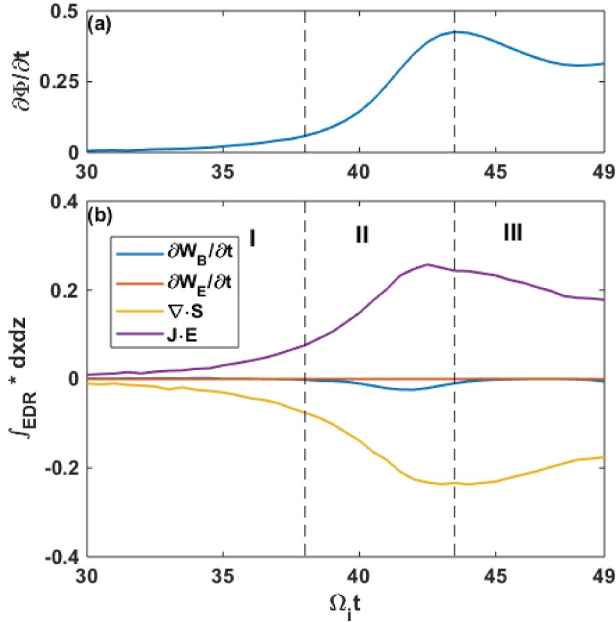


Figure 2. Time evolution of (a) reconnection rate and (b) integration of energy conversion equations in electromagnetic energy (Equation 1) in the electron diffusion region. The energy converting process can be divided into three stages based on those results, that is, Stage I: $\Omega_i t = 30$ – 38 ; Stage II: $\Omega_i t = 38$ – 43 ; Stage III: $\Omega_i t > 43$. The boundaries of different stages are shown in the black dashed lines (at $\Omega_i t = 38$ and $\Omega_i t = 43$, respectively).

Equations 1–3 depict the overall energy converting process in reconnection. $W_B \equiv B^2/(2\mu_0)$ is the magnetic energy density, and $W_E \equiv \epsilon_0 E^2/2$ is the electric energy density. $\mathbf{S} \equiv \mathbf{E} \times \mathbf{B}/\mu_0$ denotes the Poynting flux. $K_\alpha \equiv m_\alpha n_\alpha V_\alpha^2/2$ is the bulk kinetic energy density of the α type of particle, where $\alpha = i, e$ presents ion or electron. V_α is the magnitude of the bulk velocity, and \mathbf{P}_α is the pressure tensor. $U_\alpha \equiv \frac{1}{2} \int m_\alpha (\mathbf{v} - \mathbf{V}_\alpha)^2 f(\mathbf{v}) d\mathbf{v}$ is the thermal energy density. $\mathbf{H}_\alpha = U_\alpha \mathbf{V}_\alpha + \mathbf{P}_\alpha \cdot \mathbf{V}_\alpha$ is the enthalpy flux. $\mathbf{Q}_\alpha \equiv \frac{1}{2} \int m_\alpha (\mathbf{v} - \mathbf{V}_\alpha)^2 (\mathbf{v} - \mathbf{V}_\alpha) f(\mathbf{v}) d\mathbf{v}$ represents the heat flux.

The integration results are shown in the following figures. Figure 2 presents the time evolution of the temporal evolution of magnetic energy conversion by integrating the terms in Equation 1. Combined with the evolution of the reconnection rate, the energy-converting process can be divided into three stages, marked by the dashed lines in Figure 2. In Stage I ranging from $\Omega_i t = 30$ to $\Omega_i t = 38$, the input Poynting flux ($\nabla \cdot \mathbf{S} < 0$) is mainly converted to plasma kinetic energy by $\mathbf{J} \cdot \mathbf{E}$. In Stage II, the local magnetic energy in the EDR begins to drop ($\partial W_B/\partial t < 0$) at $\Omega_i t = 38$. After the peak of the reconnection rate at $\Omega_i t = 43$, it comes to Stage III. The magnetic field in the EDR is almost depleted; thus, the major energy converting pattern resembles that in Stage I again. The change of electric energy can be neglected compared with other terms.

Similarly, we show the integration of electron and ion energy conversion equations in Figures 3 and 4, respectively. For electrons, energy gained through work by the electric field $\mathbf{J}_e \cdot \mathbf{E}$ is mainly converted to outflowing

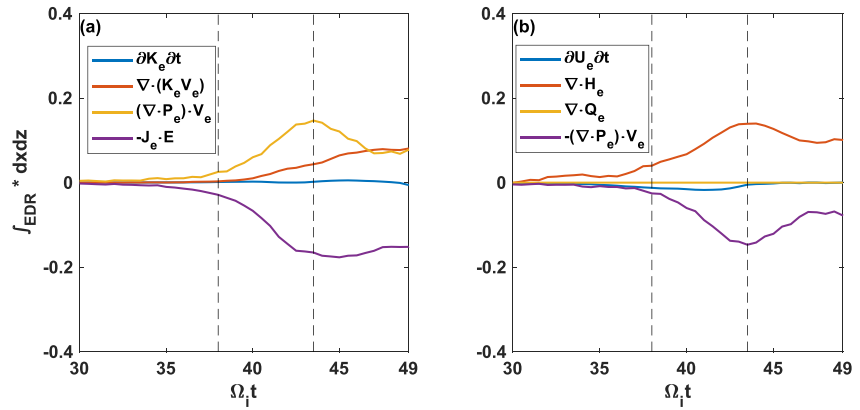


Figure 3. The integration of terms in the electron energy conversion equations (Equations 2 and 3) over time. (a) The bulk kinetic energy conversion. (b) The thermal energy conversion. The dashed lines mark different stages of energy conversion, the same as in Figure 2.

enthalpy flux via work by the pressure gradient force $-(\nabla \cdot \mathbf{P}_e) \cdot \mathbf{V}_e$. The outflow of bulk kinetic flux rises a bit in Stage II and Stage III but is smaller than the former two terms most of the time. Work by the electron pressure gradient force and the local thermal energy are together converted to the electron enthalpy flux flowing out of the EDR (see the red line in Figure 3b). The heat flux is negligible.

As for ions, the bulk kinetic energy flux is significant, especially in Stage II, while the work by the electric field $\mathbf{J}_i \cdot \mathbf{E}$ is comparable with the local kinetic energy drop (see Figure 4a). The ion thermal energy also predominantly flows out of the EDR in the form of the ion enthalpy flux, but it is not mainly attributed to the pressure gradient force (Figure 4b).

Although the overall energy conversion pattern in the EDR maintains qualitatively consistent with previous results in the broader vicinity of the X-line (Shu et al., 2021), the ratio of electron energy gain ($\int \mathbf{J}_e \cdot \mathbf{E} dV$) in the EDR can be larger than ion energy gain ($\int \mathbf{J}_i \cdot \mathbf{E} dV$) (see the purple lines in Figures 3a and 4a). This suggests the major current carrier is the electron in the EDR, which is in accord with features of thin current sheets (Artemyev et al., 2009; Asano et al., 2003; S. Lu et al., 2020). Similar results also show that electron energy gain becomes dominant in the exponential growth phase of reconnection (Payne et al., 2024). In contrast, the situation is different and the ion energy gain dominates in a wider range, that is, the ion diffusion region (IDR) as ion current density is more prominent in the IDR, as shown in previous studies (Chang et al., 2024; Shu et al., 2021). This suggests that the majority of ions gain energy from the outer region instead of the EDR. It can be seen in the following section that a large amount of ions flow out of the box, forming the enormous outflow energy flux.

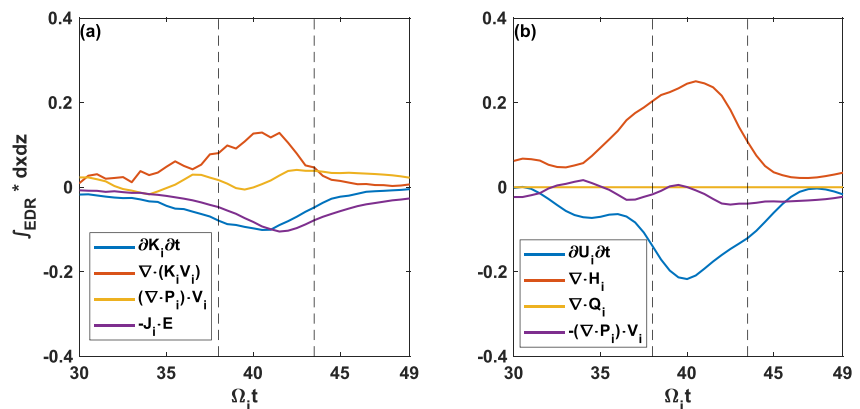


Figure 4. The integration of terms in the ion energy conversion equations (Equations 2 and 3) over time. (a) The bulk kinetic energy conversion. (b) The thermal energy conversion. The dashed lines mark different stages of energy conversion, the same as in Figure 2.

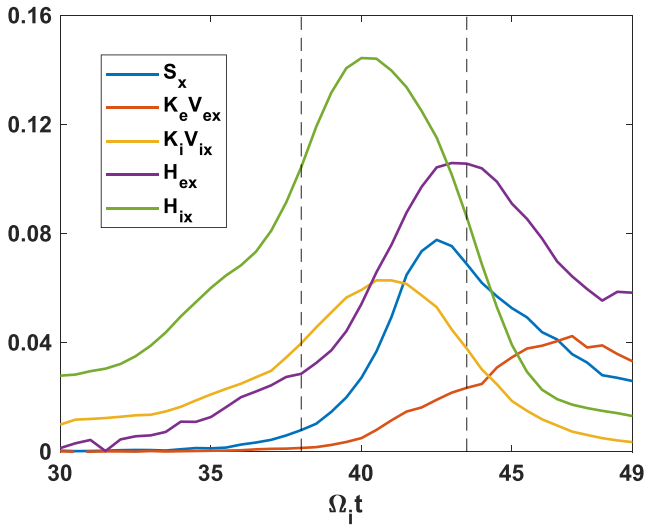


Figure 5. The energy flux flowing out from the right boundary of the box at the electron diffusion region. The dashed lines mark different stages of energy conversion, the same as in Figure 2.

3.2. Energy Flux in the Outflow Region

It holds in steady-state models that $V_{in}L \approx V_{out}\delta$ in the diffusion regions (Y. H. Liu et al., 2017, 2022; S. Wang & Lu, 2019), where V_{in} denotes the inflow velocity of plasma entering the diffusion region and V_{out} denotes the outflow velocity exiting the diffusion region. L and δ are the characteristic length and width of the diffusion region, respectively. Only under the assumption of steady state and incompressibility the equation is valid. However, the elongation of the diffusion region and pileup of the reconnected magnetic field can break those assumptions in non-steady-state cases. The energy flux in the outflow direction can well reflect this distinction.

It can be seen in Figure 5 that the outflows of the ion enthalpy flux H_{ix} and the ion bulk kinetic energy flux $K_i V_{ix}$ are dominant in Stage I and early period of Stage II (before $\Omega_i t = 40$). As suggested in Section 3.1, the ions cannot be restricted in this region as they are already unmagnetized in the IDR. The original ions in the current sheet run away as the topology of the magnetic field changes during reconnection. When most of the ions are depleted, the ion outflows drop in Stage II. The peak of the electron enthalpy flux H_{ex} lags behind that of the ion enthalpy flux. The $K_e V_{ex}$ flux rises later than other fluxes and peaks in Stage III; we will discuss this problem in Section 3.3.

Apart from the energy fluxes of particles, it is noticeable that the outflow of Poynting flux S_x arises since Stage II (the blue line in Figure 5). Even though the input of Poynting flux overwhelms the output part throughout the reconnection process ($\int_{EDR} \nabla \cdot \mathbf{S} dV < 0$ in Figure 2b), the Poynting flux outflow in Figure 5 indicates that not 100% of Poynting flux input is converted to particle energy fluxes. There is still a proportion of Poynting flux flowing out of the EDR, corresponding to the process of pileup and downstream propagation of reconnected magnetic field lines (see the B_z component in Figures 1 and b1–b4). This outflow of S_x since Stage II breaks the previous balance between the Poynting flux input and energy conversion $\mathbf{J} \cdot \mathbf{E}$, resulting in the local magnetic energy decrease in Stage II ($\int_{EDR} \partial W_B / \partial t dV < 0$ in Figure 2b).

The results above show different types of energy flux outflow at the right boundary of the EDR peak in Stage II (except the electron bulk kinetic energy). It suggests that the parameters of particles and fields cannot be steady-state during the reconnection process, which also confirms that Stage II is a vital period for the fast reconnection rate to rise and for energy to be released.

As the magnetic energy in the EDR decreases in Stage II, electrons and ions are also depleted (see the black solid lines in Figures 6a and 6b). By calculating the average translational bulk kinetic energy and the average temperature (Figures 6c and 6d), we found that although the number density in the EDR decreases, the electrons and ions are still accelerated and heated, especially in Stage II. The average electron bulk kinetic energy is an exception again as the acceleration of electrons continues in Stage III, which is consistent with the $K_e V_{ex}$ flux in Figure 5.

3.3. Particle Velocity Distribution in the EDR

By calculating $P_{e\perp}/P_{e\parallel} - 1$ shown in the left column in Figure 7, we show that electrons become anisotropic at the vicinity of the X-line as reconnection proceeds. In the inflow region, strong electron anisotropy ($P_{e\parallel} > P_{e\perp}$) develops due to electron trapping (Egedal et al., 2013). There also exists electron anisotropy in the EDR where $P_{e\perp} > P_{e\parallel}$ since Stage II (See Figures 7 and b1–d1). Apart from the EDR, the exhaust region also becomes significantly anisotropic as reconnection proceeds, which has been discussed in Shuster et al., 2014. Meanwhile, the electron agyrotropy also gradually emerges near the X-line (right column in Figure 7). Here we use $A\mathcal{O}_e \equiv 2|P_{e\perp 1} - P_{e\perp 2}|/(P_{e\perp 1} + P_{e\perp 2})$ to measure the electron agyrotropy (Karimabadi et al., 2007; Scudder & Daughton, 2008; Swisdak, 2016). It can be seen that strong agyrotropy develops in the IDR and expands to the separatrices over time during Stage II.

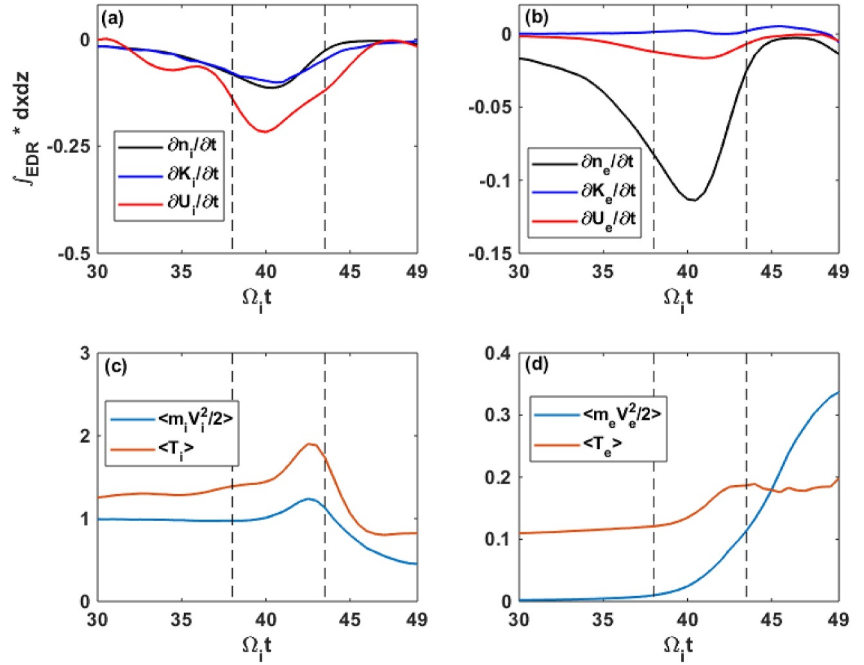


Figure 6. Time evolution of particle depletion and energization in the electron diffusion region (EDR). (a) and (b) time derivative of ion/electron number density, kinetic energy, and thermal energy. (c) and (d) the average translational kinetic energy $\langle m_\alpha V_\alpha^2/2 \rangle$ and the average temperature $\langle T_\alpha \rangle$ of ions/electrons. $\langle f_\alpha \rangle = \int_{EDR} n_\alpha f_\alpha dV / \int_{EDR} n_\alpha dV$, where f_α is an arbitrary quantity of the α type particle ($\alpha = i, e$) in EDR. The dashed lines mark different stages of energy conversion, the same as in Figure 2.

Those results indicate that using temperature as a scalar cannot well reflect particle behavior when they are accelerated and heated in the EDR. To illustrate the process of particle energization during Stage II, we present particle velocity distribution at different times below.

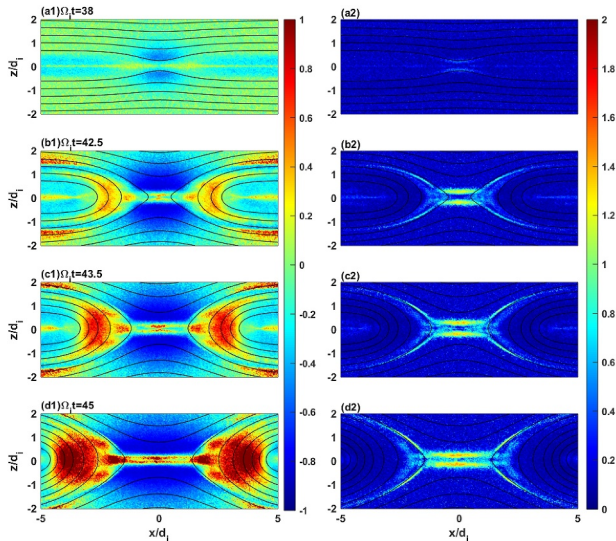


Figure 7. Electron anisotropy $P_{e\perp}/P_{e\parallel} - 1$ (left column) and agyrotropy A_{ϕ_e} (right column) at different times ($\Omega_i t = 38, 42.5, 43.5, 45$).

Figure 8 shows the electron velocity distribution near the X-line. Before Stage II, the electron distribution function is slightly anisotropic, which shows an elongation in v_x . When entering Stage II, the electron density drops evidently, consistent with the results in Figure 6b. Since $\Omega_i t = 42.5$, the electron velocity function becomes more anisotropic, forming a triangular distribution in $v_x - v_y$ plane and two portions of $+v_z$ and $-v_z$. The electrons bounce in the z -direction and are accelerated in the y -direction, corresponding to the meandering motion near the neutral line and acceleration by the out-of-plane E_y component (Bessho et al., 2014; Ng et al., 2011, 2012; Speiser, 1965). Back to our analysis of energy conversion, the broadening of the distribution function in velocity space contributes to the rise of thermal energy. Besides, it should be noted that the electron acceleration lasts until Stage III, which is consistent with the sustaining kinetic energy increase shown in Figure 6d.

Similar results of electrons at the outflow region are shown in Figure 9. Before Stage II ($\Omega_i t = 38$), there exists a large portion of backflow ($-x$ -direction), which can counteract part of the outflow of bulk kinetic energy flux, lowering the net outflow of bulk kinetic energy flux. At later times ($\Omega_i t \geq 42.5$), electrons with $-v_y$ velocity are driven outward by the Lorentz force due to the pileup magnetic field component B_z . The triangular structure of $v_x - v_y$ distribution is formed and tilted toward the $+x$ -direction as the electrons propagate downstream. As a result, the backflowing electrons are

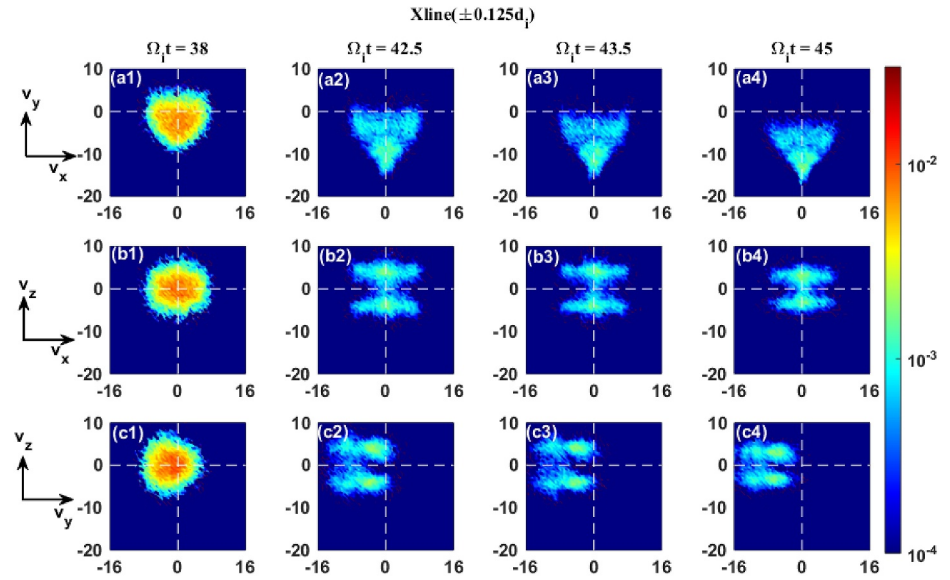


Figure 8. Electron velocity distribution $f/(n_0 V_A^2)$ in the $v_x - v_y$ plane, $v_x - v_z$ plane, and $v_y - v_z$ plane at the X-line ($x = -0.125d_i \sim 0.125d_i$; $z = -0.125d_i \sim 0.125d_i$) at $\Omega_i t = 38, 42.5, 43.5,$ and 45 .

reduced gradually. Until Stage III, the bulk kinetic energy flux outflow $K_e V_{ex}$ finally develops to a maximum (see Figure 5).

Unlike electrons, ions cannot be trapped in the EDR, as they are already unmagnetized. The ion velocity distribution is approximately uniform in the EDR. Hence, we sample the ions in the whole EDR to present the ion velocity distributions in Figure 10. Before Stage II ($\Omega_i t = 38$), the ions show a crescent distribution in the $v_y - v_z$ plane (Figure 10c1), indicating the meandering motion around the neutral line, even though the characteristic length of the ion meandering path can be larger than the range of EDR (S. Wang et al., 2016). Most of the ions are populated in $+v_y$ direction at this time. However, when entering Stage II, the ions with $+v_y$ velocity are propelled by the Lorentz force due to the reconnected magnetic field B_z and run away from the EDR, resulting in the

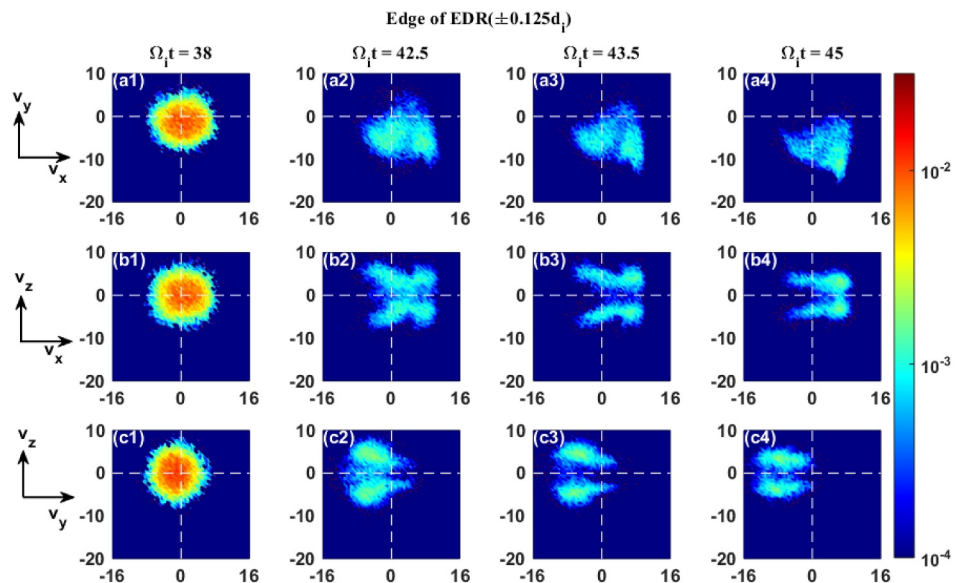


Figure 9. Electron velocity distribution $f/(n_0 V_A^2)$ in the $v_x - v_y$ plane, $v_x - v_z$ plane, and $v_y - v_z$ plane at the right edge of the electron diffusion region ($x = 0.575d_i \sim 0.825d_i$; $z = -0.125d_i \sim 0.125d_i$) at $\Omega_i t = 38, 42.5, 43.5,$ and 45 .

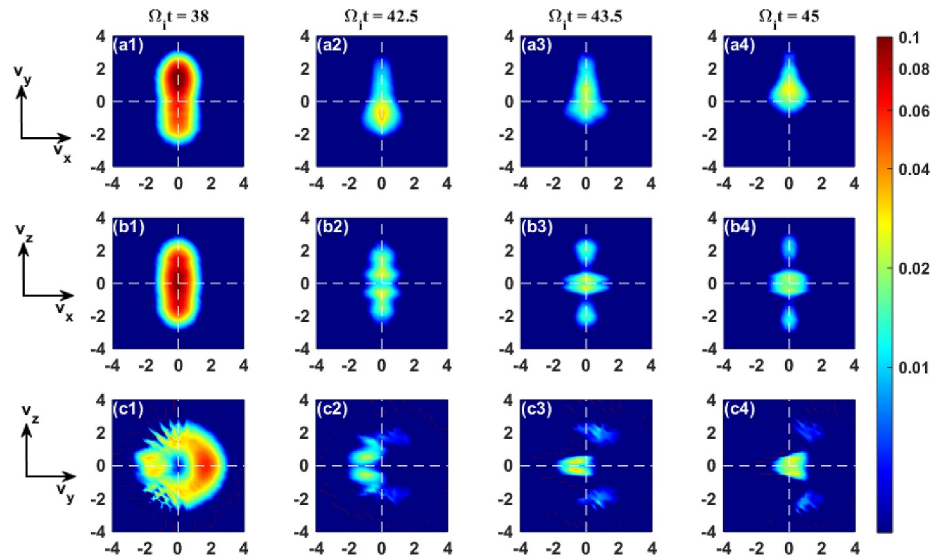


Figure 10. Ion velocity distribution $f/(n_0 V_A^2)$ in the $v_x - v_y$ plane, $v_x - v_z$, and $v_y - v_z$ plane in the electron diffusion region ($x = -0.7 \sim 0.7 d_i$; $z = -0.375 d_i \sim 0.375 d_i$) at $\Omega_i t = 38, 42.5, 43.5,$ and 45 .

massive outflow of ion energy flux shown in Figure 5. The remaining part with $-v_y$ is gradually turning to $+v_y$ direction by the reconnection electric field and also runs away in later times.

4. Conclusions and Discussion

In this paper, we present the temporal evolution of energy conversion in the EDR of non-steady-state reconnection. We find that the energy conversion pattern shows distinct features at different stages. Those features are (a) the local magnetic energy depletion during Stage II, characterized by the sharp rise of the reconnection rate, generating the Poynting flux outflow in the exhaust region; (b) particle energization and runaway occurring at the same time (also most drastically in Stage II); (c) prominent and evolving particle anisotropy emerging in Stage II. Therefore, we suggest the non-steady-state feature of energy conversion in magnetic reconnection is vital to the time evolution of the fast reconnection rate.

When the energy is depleted near the X-line (Figure 6), the balance between the thermal pressure and the outer magnetic pressure is broken, urging the upstream magnetic field lines along with the plasmas to flow into the diffusion region. As a result, the reconnection process is expedited. The previous study (Li & Liu, 2021) has also shown that the thermal pressure can modify the reconnection rate and the outflow velocity by affecting the force balance around the diffusion region. Despite the drastic change in the EDR during this period, it is surprising that the size of the inner EDR remains almost unchanged. This suggests the geometry of the diffusion region remains approximately stable so that previous steady-state models of reconnection rate may be applied to the non-steady-state case to some extent with further modification. Similar results have also been found in driven reconnection (Wan & Lapenta, 2008). It should be pointed out that in driven reconnection, the reconnection process is determined by the driven force. Hence, the researchers claimed that reconnection is not controlled by the downstream physics. However, in our simulation of spontaneous reconnection, it is found that the downstream outflow and the pileup magnetic reconnection can influence the evolution of fast reconnection because the free energy in spontaneous reconnection does not come from the upstream-driven power but from the current sheet itself.

The structure of electron velocity distribution (shown in Figures 8 and 9) and corresponding motions in the EDR have also been reported by the Magnetospheric Multiscale (MMS) satellite observations (Li et al., 2019; Torbert et al., 2018) and are also illustrated in simulations (Bessho et al., 2014, 2016; Bourdin, 2017; S. Lu et al., 2019; Ng et al., 2011, 2012). Those results indicate the electrons are energized in the diffusion region (X. R. Fu et al., 2006; Hoshino, 2022; C. Huang et al., 2010; Shay et al., 2014). Those electrons following the meandering motion are trapped in the EDR and are firstly energized in the $-z$ -direction by the reconnection electric field. Then they are diverted downstream by the reconnected magnetic field B_z . The large electron energy flux dominated by the out-

of-plane component in the vicinity of the EDR is also observed in asymmetric magnetopause reconnection by MMS (Eastwood et al., 2020). It is shown in the observation that the electron energy flux is highly structured and filamentary and the electron enthalpy flux is larger than the electron bulk kinetic energy flux, which is consistent with our results (see Figure 5). The difference is that the ion heat flux is observable in observation while negligible in our simulation. The temperature gradient is likely to be large in the asymmetric reconnection observed in the magnetopause. On the other hand, the temperature is initially uniform in the simulation setup. Thus it is hard for the heat flux to rise in our results.

The ion energization cannot be well reflected in our results as we mainly focus on the EDR where most ions straightly run away (Figure 10). Besides, the initial ion temperature is much higher than the electron temperature, meaning the original ion thermal energy and drift velocity in the y -direction (due to the limitation of Harris equilibrium) are large. Hence the ion heating or acceleration can be harder to observe than colder electrons. Outside the inner EDR, ion motion is controlled by the Lorentz force, the thermal pressure gradient, and the Hall electric field. The combination of three forces continuously accelerates the ion in the x -direction until the dipolarization front (Chang et al., 2024). Still, ion energization is found in observations (Priest et al., 1998; Runov et al., 2017; Zhou et al., 2010), experiments (Hare et al., 2017; Hsu et al., 2000; Magee et al., 2011; Ono et al., 1996, 2011), and simulations (Aunai et al., 2011; Drake & Swisdak, 2012; S. Lu et al., 2019; S. Wang et al., 2016; Yoon et al., 2023).

We set a thin current sheet without any perturbation at initialization so that the collisionless tearing mode can be triggered spontaneously. Our results show that evident energy conversion emerges when the nonlinear explosive stage of reconnection begins (Stage II in Figure 2). The onset of fast magnetic reconnection is a heated topic. Spacecraft observations and simulations have shown that fast reconnection starts from small scales controlled by electron kinetics (S. Lu et al., 2020). In a more realistic situation with a thick current sheet, the current sheet starts thinning in the linear phase of collisionless tearing instability, which can be quite slow and its energy dissipation is negligible according to the linear theory. Fast reconnection is triggered only after the thickness of the current sheet reaches the electron scale (Daughton et al., 2009; D. Liu et al., 2020). Previous studies indicate the process can be expedited either by a strong external driver (S. Lu et al., 2020) or the inertia resistivity provided by the reconnecting magnetic field (Hoshino, 2021). According to Hoshino (2021), the thickness of the current sheet can drop quickly to the electron scale during the nonlinear stage of the tearing instability within tens of the Alfvén transit time. Thereafter, the energy-converting process of reconnection can begin.

Although reconnection is triggered in the EDR and provides the first acceleration of electrons, the EDR contributes a minor proportion to the overall energy conversion during the reconnection process (Birn & Hesse, 2005). The major energy-converting process occurs at the dipolarization front (Shu et al., 2021; Yi et al., 2019). The two energy-converting regions are connected by the Poynting flux outflowing from the EDR (as shown in Figure 1d). As the reconnected magnetic field piles up and propagates downstream, the electric field is enhanced and exceeds the reconnection electric field at the X -line (Q. Lu et al., 2013). The electric field at the propagating dipolarization front contributes to further energy conversion in this region. In this way, the energy conversion at the dipolarization front can be linked to the process in the EDR.

Data Availability Statement

The simulation data for the figures in the paper can be downloaded from <https://doi.org/10.57760/sciencedb.14434> (Shu, 2024).

References

- Angelopoulos, V., McFadden, J. P., Larson, D., Carlson, C. W., Mende, S. B., Frey, H., et al. (2008). Tail reconnection triggering substorm onset. *Science*, *321*(5891), 931–935. <https://doi.org/10.1126/science.1160495>
- Angelopoulos, V., Runov, A., Zhou, X.-Z., Turner, D. L., Kiehas, S. A., Li, S.-S., & Shinohara, I. (2013). Electromagnetic energy conversion at reconnection fronts. *Science*, *341*(6153), 1478–1482. <https://doi.org/10.1126/science.1236992>
- Arber, T. D., Bennett, K., Brady, C. S., Lawrence-Douglas, A., Ramsay, M. G., Sircombe, N. J., et al. (2015). Contemporary particle-in-cell approach to laser-plasma modelling. *Plasma Physics and Controlled Fusion*, *57*(11), 113001. <https://doi.org/10.1088/0741-3335/57/11/113001>
- Artemyev, A. V., Petrukovich, A. A., Zelenyi, L. M., Nakamura, R., Malova, H. V., & Popov, V. Y. (2009). Thin embedded current sheets: Cluster observations of ion kinetic structure and analytical models. *Annales Geophysicae*, *27*(10), 4075–4087. <https://doi.org/10.5194/angeo-27-4075-2009>
- Asano, Y., Mukai, T., Hoshino, M., Saito, Y., Hayakawa, H., & Nagai, T. (2003). Evolution of the thin current sheet in a substorm observed by Geotail. *Journal of Geophysical Research*, *108*(A5), 1–10. <https://doi.org/10.1029/2002JA009785>

Acknowledgments

This research was funded by the Strategic Priority Research Program of Chinese Academy of Sciences (Grants XDB0560000). This work utilized the EPOCH PIC code, which was in part funded by the UK EPSRC grants EP/G054950/1, EP/G056803/1, EP/G055165/1 and EP/M022463/1. Computer resources were provided by the Hefei Advanced Computing Center of China. Grateful acknowledgment is made to the data resources from “National Space Science Data Center, National Science and Technology Infrastructure of China (<http://www.nssdc.ac.cn>).”

- Aunai, N., Belmont, G., & Smets, R. (2011). Energy budgets in collisionless magnetic reconnection: Ion heating and bulk acceleration. *Physics of Plasmas*, 18(12), 122901. <https://doi.org/10.1063/1.3664320>
- Baker, D. N., Pulkkinen, T. I., Angelopoulos, V., Baumjohann, W., & McPherron, R. L. (1996). Neutral line model of substorms: Past results and present view. *Journal of Geophysical Research*, 101(A6), 12975–13010. <https://doi.org/10.1029/95JA03753>
- Bárta, M., Büchner, J., Karlický, M., & Kotrč, P. (2011). Spontaneous current-layer fragmentation and cascading reconnection in solar flares. II. Relation to observations. *The Astrophysical Journal*, 730(1), 47. <https://doi.org/10.1088/0004-637X/730/1/47>
- Bessho, N., Chen, L.-J., & Hesse, M. (2016). Electron distribution functions in the diffusion region of asymmetric magnetic reconnection. *Geophysical Research Letters*, 43(5), 1828–1836. <https://doi.org/10.1002/2016GL067886>
- Bessho, N., Chen, L.-J., Shuster, J. R., & Wang, S. (2014). Electron distribution functions in the electron diffusion region of magnetic reconnection: Physics behind the fine structures. *Geophysical Research Letters*, 41(24), 8688–8695. <https://doi.org/10.1002/2014GL062034>
- Bessho, N., Chen, L.-J., Wang, S., & Hesse, M. (2018). Effect of the reconnection electric field on electron distribution functions in the diffusion region of magnetotail reconnection. *Geophysical Research Letters*, 45(22), 12142–12152. <https://doi.org/10.1029/2018GL081216>
- Birn, J., & Hesse, M. (2005). Energy release and conversion by reconnection in the magnetotail. *Annales Geophysicae*, 23(10), 3365–3373. <https://doi.org/10.5194/angeo-23-3365-2005>
- Birn, J., & Hesse, M. (2010). Energy release and transfer in guide field reconnection. *Physics of Plasmas*, 17(1), 1–11. <https://doi.org/10.1063/1.3299388>
- Bourdin, P. A. (2017). Catalog of fine-structured electron velocity distribution functions -Part I: Antiparallel magnetic-field reconnection (Geospace Environmental Modeling case). *Annales Geophysicae*, 35(5), 1051–1067. <https://doi.org/10.5194/angeo-35-1051-2017>
- Burch, J. L., & Phan, T. D. (2016). Magnetic reconnection at the dayside magnetopause: Advances with MMS. *Geophysical Research Letters*, 43(16), 8327–8338. <https://doi.org/10.1002/2016GL069787>
- Cassak, P. A., Liu, Y. H., & Shay, M. A. A. (2017). A review of the 0.1 reconnection rate problem. *Journal of Plasma Physics*, 83(5), 1–17. <https://doi.org/10.1017/S0022377817000666>
- Cazzola, E., Innocenti, M. E., Goldman, M. V., Newman, D. L., Markidis, S., & Lapenta, G. (2016). On the electron agyrotropy during rapid asymmetric magnetic island coalescence in presence of a guide field. *Geophysical Research Letters*, 43(15), 7840–7849. <https://doi.org/10.1002/2016GL070195>
- Chang, C., Lu, Q., Lu, S., Huang, K., & Wang, R. (2024). Ion and electron motions in the outer electron diffusion region of collisionless magnetic reconnection. *Earth and Planetary Physics*, 8(3), 472–478. <https://doi.org/10.26464/epp2024020>
- Daughton, W., Roytershteyn, V., Albright, B. J., Karimabadi, H., Yin, L., & Bowers, K. J. (2009). Transition from collisional to kinetic regimes in large-scale reconnection layers. *Physical Review Letters*, 103(6), 065004. <https://doi.org/10.1103/PhysRevLett.103.065004>
- Daughton, W., Scudder, J., & Karimabadi, H. (2006). Fully kinetic simulations of undriven magnetic reconnection with open boundary conditions. *Physics of Plasmas*, 13(7), 072101. <https://doi.org/10.1063/1.2218817>
- Deng, X., Ashour-Abdalla, M., Zhou, M., Walker, R., El-Alaoui, M., Angelopoulos, V., et al. (2010). Wave and particle characteristics of earthward electron injections associated with dipolarization fronts. *Journal of Geophysical Research*, 115(9), 1–14. <https://doi.org/10.1029/2009JA015107>
- Dorfman, S., Ji, H., Yamada, M., Yoo, J., Lawrence, E., Myers, C., & Tharp, T. D. (2014). Experimental observation of 3-D, impulsive reconnection events in a laboratory plasma. *Physics of Plasmas*, 21(1), 012109. <https://doi.org/10.1063/1.4862039>
- Drake, J. F., & Swisdak, M. (2012). Ion heating and acceleration during magnetic reconnection relevant to the corona. *Space Science Reviews*, 172(1–4), 227–240. <https://doi.org/10.1007/s11214-012-9903-3>
- Eastwood, J. P., Goldman, M. V., Phan, T. D., Stawarz, J. E., Cassak, P. A., Drake, J. F., et al. (2020). Energy flux densities near the electron dissipation region in asymmetric magnetopause reconnection. *Physical Review Letters*, 125(26), 265102. <https://doi.org/10.1103/PhysRevLett.125.265102>
- Eastwood, J. P., Phan, T. D., Drake, J. F., Shay, M. A., Borg, A. L., Lavraud, B., & Taylor, M. G. G. T. (2013). Energy partition in magnetic reconnection in earth's magnetotail. *Physical Review Letters*, 110(22), 225001. <https://doi.org/10.1103/PhysRevLett.110.225001>
- Egedal, J., Le, A., & Daughton, W. (2013). A review of pressure anisotropy caused by electron trapping in collisionless plasma, and its implications for magnetic reconnection. *Physics of Plasmas*, 20(6), 061201. <https://doi.org/10.1063/1.4811092>
- Fargette, N., Eastwood, J. P., Waters, C. L., Øieroset, M., Phan, T. D., Newman, D. L., et al. (2024). Statistical study of energy transport and conversion in electron diffusion regions at Earth's dayside magnetopause. *Journal of Geophysical Research: Space Physics*, 129(10), e2024JA032897. <https://doi.org/10.1029/2024JA032897>
- Fu, H. S., Cao, J. B., Khotyaintsev, Y. V., Sitnov, M. I., Runov, A., Fu, S. Y., et al. (2013). Dipolarization fronts as a consequence of transient reconnection: In situ evidence. *Geophysical Research Letters*, 40(23), 6023–6027. <https://doi.org/10.1002/2013GL058620>
- Fu, X. R., Lu, Q. M., & Wang, S. (2006). The process of electron acceleration during collisionless magnetic reconnection. *Physics of Plasmas*, 13(1), 1–7. <https://doi.org/10.1063/1.2164808>
- Fuselier, S. A., Petrinec, S. M., Sawyer, R. P., Mukherjee, J., & Masters, A. (2020). Suppression of magnetic reconnection at Saturn's Low-Latitude magnetopause. *Journal of Geophysical Research: Space Physics*, 125(5), 1–16. <https://doi.org/10.1029/2020JA027895>
- Goldman, M. V., Newman, D. L., & Lapenta, G. (2016). What can we learn about magnetotail reconnection from 2D PIC Harris-sheet simulations? *Space Science Reviews*, 199(1–4), 651–688. <https://doi.org/10.1007/s11214-015-0154-y>
- Hare, J. D., Suttle, L., Lebedev, S. V., Loureiro, N. F., Ciardi, A., Burdiak, G. C., et al. (2017). Anomalous heating and plasmoid formation in a driven magnetic reconnection experiment. *Physical Review Letters*, 118(8), 1–6. <https://doi.org/10.1103/PhysRevLett.118.085001>
- Hoshino, M. (2021). Nonlinear explosive magnetic reconnection in a collisionless system. *Physics of Plasmas*, 28(6), 062106. <https://doi.org/10.1063/5.0050389>
- Hoshino, M. (2022). Efficiency of nonthermal particle acceleration in magnetic reconnection. *Physics of Plasmas*, 29(4), 042902. <https://doi.org/10.1063/5.0086316>
- Hsu, S. C., Fiksel, G., Carter, T. A., Ji, H., Kulsrud, R. M., & Yamada, M. (2000). Local measurement of nonclassical ion heating during magnetic reconnection. *Physical Review Letters*, 84(17), 3859–3862. <https://doi.org/10.1103/PhysRevLett.84.3859>
- Huang, C., Du, A., & Ge, Y. S. (2020). Evolution of electron current layer during anti-parallel magnetic reconnection. *Plasma Physics and Controlled Fusion*, 62(5), 055014. <https://doi.org/10.1088/1361-6587/ab7d49>
- Huang, C., Lu, Q., & Wang, S. (2010). The mechanisms of electron acceleration in antiparallel and guide field magnetic reconnection. *Physics of Plasmas*, 17(7), 1–8. <https://doi.org/10.1063/1.3457930>
- Huang, K., Lu, Q., Lu, S., Wang, R., & Wang, S. (2021). Formation of Pancake, Rolling Pin, and Cigar distributions of energetic electrons at the dipolarization fronts (DFs) driven by magnetic reconnection: A two-dimensional particle-in-cell simulation. *Journal of Geophysical Research: Space Physics*, 126(10), e2021JA029939. <https://doi.org/10.1029/2021JA029939>

- Imada, S., Nakamura, R., Daly, P. W., Hoshino, M., Baumjohann, W., Mühlbacher, S., et al. (2007). Energetic electron acceleration in the downstream reconnection outflow region. *Journal of Geophysical Research*, *112*(A3), A03202. <https://doi.org/10.1029/2006JA011847>
- Karimabadi, H., Daughton, W., & Scudder, J. (2007). Multi-scale structure of the electron diffusion region. *Geophysical Research Letters*, *34*(13), 1–5. <https://doi.org/10.1029/2007GL030306>
- Kepko, L., McPherron, R. L., Amm, O., Apatenkov, S., Baumjohann, W., Birn, J., et al. (2015). Substorm current wedge revisited. *Space Science Reviews*, *190*(1–4), 1–46. <https://doi.org/10.1007/s11214-014-0124-9>
- Li, X., & Liu, Y.-H. (2021). The effect of thermal pressure on collisionless magnetic reconnection rate. *The Astrophysical Journal*, *912*(2), 152. <https://doi.org/10.3847/1538-4357/abf48c>
- Li, X., Wang, R., Lu, Q., Hwang, K. J., Zong, Q., Russell, C. T., & Wang, S. (2019). Observation of nongyrotropic electron distribution across the electron diffusion region in the magnetotail reconnection. *Geophysical Research Letters*, *46*(24), 14263–14273. <https://doi.org/10.1029/2019GL085014>
- Lin, J., & Forbes, T. G. (2000). Effects of reconnection on the coronal mass ejection process. *Journal of Geophysical Research*, *105*(A2), 2375–2392. <https://doi.org/10.1029/1999ja900477>
- Liu, D., Lu, S., Lu, Q., Ding, W., & Wang, S. (2020). Spontaneous onset of collisionless magnetic reconnection on an electron scale. *The Astrophysical Journal Letters*, *890*(2), L15. <https://doi.org/10.3847/2041-8213/ab72fe>
- Liu, Y. H., Cassak, P., Li, X., Hesse, M., Lin, S. C., & Genestreti, K. (2022). First-principles theory of the rate of magnetic reconnection in magnetospheric and solar plasmas. *Communications Physics*, *5*(1), 97. <https://doi.org/10.1038/s42005-022-00854-x>
- Liu, Y. H., Hesse, M., Guo, F., Daughton, W., Li, H., Cassak, P. A., & Shay, M. A. (2017). Why does steady-state magnetic reconnection have a maximum local rate of order 0.1? *Physical Review Letters*, *118*(8), 0–6. <https://doi.org/10.1103/PhysRevLett.118.085101>
- Lu, Q., Fu, H., Wang, R., & Lu, S. (2022). Collisionless magnetic reconnection in the magnetosphere. *Chinese Physics B*, *31*(8), 089401. <https://doi.org/10.1088/1674-1056/ac76ab>
- Lu, Q., Lu, S., Huang, C., Wu, M., & Wang, S. (2013). Self-reinforcing process of the reconnection electric field in the electron diffusion region and onset of collisionless magnetic reconnection. *Plasma Physics and Controlled Fusion*, *55*(8), 085019. <https://doi.org/10.1088/0741-3335/55/8/085019>
- Lu, S., Angelopoulos, V., Artemyev, A. V., Jia, Y., Chen, Q., Liu, J., & Runov, A. (2020). Magnetic reconnection in a charged, electron-dominant current sheet. *Physics of Plasmas*, *27*(10), 102902. <https://doi.org/10.1063/5.0020857>
- Lu, S., Angelopoulos, V., Artemyev, A. V., Pritchett, P. L., Liu, J., Runov, A., et al. (2019). Turbulence and particle acceleration in collisionless magnetic reconnection: Effects of temperature inhomogeneity across Pre-reconnection current sheet. *The Astrophysical Journal*, *878*(2), 109. <https://doi.org/10.3847/1538-4357/ab1f6b>
- Lu, S., Lu, Q., Huang, C., & Wang, S. (2013). The transfer between electron bulk kinetic energy and thermal energy in collisionless magnetic reconnection. *Physics of Plasmas*, *20*(6), 061203. <https://doi.org/10.1063/1.4811119>
- Lu, S., Lu, Q., Lin, Y., Wang, X., Ge, Y., Wang, R., et al. (2015). Dipolarization fronts as earthward propagating flux ropes: A three-dimensional global hybrid simulation. *Journal of Geophysical Research: Space Physics*, *120*(8), 6286–6300. <https://doi.org/10.1002/2015JA021213>
- Lu, S., Wang, R., Lu, Q., Angelopoulos, V., Nakamura, R., Artemyev, A. V., et al. (2020). Magnetotail reconnection onset caused by electron kinetics with a strong external driver. *Nature Communications*, *11*(1), 1–7. <https://doi.org/10.1038/s41467-020-18787-w>
- Magee, R. M., Den Hartog, D. J., Kumar, S. T. A., Almagri, A. F., Chapman, B. E., Fiksel, G., et al. (2011). Anisotropic ion heating and tail generation during tearing mode magnetic reconnection in a high-temperature plasma. *Physical Review Letters*, *107*(6), 1–5. <https://doi.org/10.1103/PhysRevLett.107.065005>
- Nagayama, Y., Yamada, M., Park, W., Fredrickson, E. D., Janos, A. C., McGuire, K. M., & Taylor, G. (1996). Tomography of full sawtooth crashes on the tokamak fusion test reactor. *Physics of Plasmas*, *3*(5), 1647–1655. <https://doi.org/10.1063/1.872025>
- Ng, J., Egedal, J., Le, A., & Daughton, W. (2012). Phase space structure of the electron diffusion region in reconnection with weak guide fields. *Physics of Plasmas*, *19*(11), 112108. <https://doi.org/10.1063/1.4766895>
- Ng, J., Egedal, J., Le, A., Daughton, W., & Chen, L. J. (2011). Kinetic structure of the electron diffusion region in antiparallel magnetic reconnection. *Physical Review Letters*, *106*(6), 1–4. <https://doi.org/10.1103/PhysRevLett.106.065002>
- Ono, Y., Tanabe, H., Hayashi, Y., Ii, T., Narushima, Y., Yamada, T., et al. (2011). Ion and electron heating characteristics of magnetic reconnection in a two flux loop merging experiment. *Physical Review Letters*, *107*(18), 185001. <https://doi.org/10.1103/PhysRevLett.107.185001>
- Ono, Y., Yamada, M., Akao, T., Tajima, T., & Matsumoto, R. (1996). Ion acceleration and direct ion heating in three-component magnetic reconnection. *Physical Review Letters*, *76*(18), 3328–3331. <https://doi.org/10.1103/PhysRevLett.76.3328>
- Payne, D. S., Torbert, R. B., Germaschewski, K., Forbes, T. G., & Shuster, J. R. (2024). Relating the phases of magnetic reconnection growth to energy transport mechanisms in the exhaust. *Journal of Geophysical Research: Space Physics*, *129*(5), e2023JA032015. <https://doi.org/10.1029/2023JA032015>
- Priest, E. R., Foley, C. R., Heyvaerts, J., Arber, T. D., Culhane, J. L., & Actons, L. W. (1998). Nature of the heating mechanisms for the diffuse solar corona. *Nature*, *393*(6685), 545–547. <https://doi.org/10.1038/311166>
- Ren, Y., Yamada, M., Gerhardt, S., Ji, H., Kulsrud, R., & Kuritsyn, A. (2005). Experimental verification of the Hall effect during magnetic reconnection in a laboratory plasma. *Physical Review Letters*, *95*(5), 055003. <https://doi.org/10.1103/PhysRevLett.95.055003>
- Runov, A., Angelopoulos, V., Artemyev, A., Birn, J., Pritchett, P. L., & Zhou, X. Z. (2017). Characteristics of ion distribution functions in dipolarizing flux bundles: Event studies. *Journal of Geophysical Research: Space Physics*, *122*(6), 5965–5978. <https://doi.org/10.1002/2017JA024010>
- Runov, A., Angelopoulos, V., Sitnov, M., Sergeev, V. A., Nakamura, R., Nishimura, Y., et al. (2011). Dipolarization fronts in the magnetotail plasma sheet. *Planetary and Space Science*, *59*(7), 517–525. <https://doi.org/10.1016/j.pss.2010.06.006>
- Sang, L., Lu, Q., Xie, J., Fan, F., Zhang, Q., Ding, W., et al. (2022). Energy dissipation during magnetic reconnection in the Keda linear magnetized plasma device. *Physics of Plasmas*, *29*(10), 102108. <https://doi.org/10.1063/5.0090790>
- Scudder, J., & Daughton, W. (2008). Illuminating electron diffusion regions of collisionless magnetic reconnection using electron agyrotropy. *Journal of Geophysical Research*, *113*(6), A06222. <https://doi.org/10.1029/2008JA013035>
- Shay, M. A., Drake, J. F., Rogers, B. N., & Denton, R. E. (1999). The scaling of collisionless, magnetic reconnection for large systems. *Geophysical Research Letters*, *26*(14), 2163–2166. <https://doi.org/10.1029/1999GL900481>
- Shay, M. A., Drake, J. F., & Swisdak, M. (2007). Two-scale structure of the electron dissipation region during collisionless magnetic reconnection. *Physical Review Letters*, *99*(15), 155002. <https://doi.org/10.1103/PhysRevLett.99.155002>
- Shay, M. A., Haggerty, C. C., Phan, T. D., Drake, J. F., Cassak, P. A., Wu, P., et al. (2014). Electron heating during magnetic reconnection: A simulation scaling study. *Physics of Plasmas*, *21*(12), 1–11. <https://doi.org/10.1063/1.4904203>
- Shu, Y. (2024). Evolution of energy conversion and particle behaviour in the electron diffusion region during non-steady-state magnetic reconnection[DS/OL]. V1. *Science Data Bank*. <https://doi.org/10.57760/sciencedb.14434>

- Shu, Y., Lu, S., Lu, Q., Ding, W., & Wang, S. (2021). Energy budgets from collisionless magnetic reconnection site to reconnection front. *Journal of Geophysical Research: Space Physics*, *126*(10), e2021JA029712. <https://doi.org/10.1029/2021JA029712>
- Shu, Y., Lu, S., Lu, Q., Wang, R., Zheng, J., & Ding, W. (2022). Effects of guide field and background density and temperature on energy conversion at magnetic reconnection front. *Journal of Geophysical Research: Space Physics*, *127*(9), 1–12. <https://doi.org/10.1029/2022JA030546>
- Shuster, J. R., Chen, L. J., Daughton, W. S., Lee, L. C., Lee, K. H., Bessho, N., et al. (2014). Highly structured electron anisotropy in collisionless reconnection exhausts. *Geophysical Research Letters*, *41*(15), 5389–5395. <https://doi.org/10.1002/2014GL060608>
- Sitnov, M. I., Swisdak, M., & Divin, A. V. (2009). Dipolarization fronts as a signature of transient reconnection in the magnetotail. *Journal of Geophysical Research*, *114*(A4), A04202. <https://doi.org/10.1029/2008ja013980>
- Speiser, T. W. (1965). Particle trajectories in model current sheets: 1. Analytical solutions. *Journal of Geophysical Research*, *70*(17), 4219–4226. <https://doi.org/10.1029/JZ070i017p04219>
- Swisdak, M. (2016). Quantifying gyrotropy in magnetic reconnection. *Geophysical Research Letters*, *43*(1), 43–49. <https://doi.org/10.1002/2015GL066980>
- Takasao, S., Asai, A., Isobe, H., & Shibata, K. (2012). Simultaneous observation of reconnection inflow and outflow associated with the 2010 August 18 solar flare. *The Astrophysical Journal*, *745*(1), L6. <https://doi.org/10.1088/2041-8205/745/1/L6>
- Tharp, T. D., Yamada, M., Ji, H., Lawrence, E., Dorfman, S., Myers, C. E., & Yoo, J. (2012). Quantitative study of guide-field effects on Hall reconnection in a laboratory plasma. *Physical Review Letters*, *109*(16), 165002. <https://doi.org/10.1103/PhysRevLett.109.165002>
- Torbert, R. B., Burch, J. L., Phan, T. D., Hesse, M., Argall, M. R., Shuster, J., et al. (2018). Electron-scale dynamics of the diffusion region during symmetric magnetic reconnection in space. *Science*, *362*(6421), 1391–1395. <https://doi.org/10.1126/science.aat2998>
- Wan, W., & Lapenta, G. (2008). Evolutions of non-steady-state magnetic reconnection. *Physics of Plasmas*, *15*(10), 102302. <https://doi.org/10.1063/1.2991406>
- Wang, L., Huang, C., Cao, X., Du, A., & Ge, Y. S. (2020). Magnetic energy conversion and transport in the terrestrial magnetotail due to dipolarization fronts. *Journal of Geophysical Research: Space Physics*, *125*(10), 1–11. <https://doi.org/10.1029/2020JA028568>
- Wang, R., Lu, Q., Du, A., & Wang, S. (2010). In situ observations of a secondary magnetic island in an ion diffusion region and associated energetic electrons. *Physical Review Letters*, *104*(17), 2–5. <https://doi.org/10.1103/PhysRevLett.104.175003>
- Wang, S., Chen, L. J., Hesse, M., Bessho, N., Gershman, D. J., Dorelli, J., et al. (2016). Two-scale ion meandering caused by the polarization electric field during asymmetric reconnection. *Geophysical Research Letters*, *43*(15), 7831–7839. <https://doi.org/10.1002/2016GL069842>
- Wang, S., & Lu, Q. (2019). Collisionless magnetic reconnection (in Chinese). Science Press.
- Wang, S., Wang, R., Lu, Q., Fu, H., & Wang, S. (2020). Direct evidence of secondary reconnection inside filamentary currents of magnetic flux ropes during magnetic reconnection. *Nature Communications*, *11*(1), 3964. <https://doi.org/10.1038/s41467-020-17803-3>
- Wesson, J. A. (1990). Sawtooth reconnection. *Nuclear Fusion*, *30*(12), 2545–2549. <https://doi.org/10.1088/0029-5515/30/12/008>
- Yamada, M., Levinton, F. M., Pomphrey, N., Budny, R., Manickam, J., & Nagayama, Y. (1994). Investigation of magnetic reconnection during a sawtooth crash in a high-temperature tokamak plasma. *Physics of Plasmas*, *1*(10), 3269–3276. <https://doi.org/10.1063/1.870479>
- Yamada, M., Yoo, J., Jara-Almonte, J., Ji, H., Kulsrud, R. M., & Myers, C. E. (2014). Conversion of magnetic energy in the magnetic reconnection layer of a laboratory plasma. *Nature Communications*, *5*(May), 4774. <https://doi.org/10.1038/ncomms5774>
- Yi, Y., Zhou, M., Song, L., & Deng, X. (2019). On the energy conversion rate during collisionless magnetic reconnection. *The Astrophysical Journal Letters*, *883*(1), L22. <https://doi.org/10.3847/2041-8213/ab40c1>
- Yoon, Y. D., Bellan, P. M., & Yun, G. S. (2023). Phase-space analysis of ordered and disordered nonthermal ion energization during magnetic reconnection. *The Astrophysical Journal*, *956*(2), 105. <https://doi.org/10.3847/1538-4357/acf1f5>
- Zhou, X. Z., Angelopoulos, V., Sergeev, V. A., & Runov, A. (2010). Accelerated ions ahead of earthward propagating dipolarization fronts. *Journal of Geophysical Research*, *115*(9), 1–8. <https://doi.org/10.1029/2010JA015481>